

Resonances Formed by $\bar{p}p$ and Decaying into $\pi^0\pi^0\eta$ for Masses 1960 to 2410 MeV

A.V. Anisovich^c, C.A. Baker^a, C.J. Batty^a, D.V. Bugg^b, C. Hoddd^b, J. Kisiel^d, V.A. Nikonov^c, A.V. Sarantsev^c,
V.V. Sarantsev^c, I. Scott^b, B.S. Zou^b¹

^a *Rutherford Appleton Laboratory, Chilton, Didcot OX11 0QX, UK*

^b *Queen Mary and Westfield College, London E1 4NS, UK*

^c *PNPI, Gatchina, St. Petersburg district, 188350, Russia*

^d *University of Silesia, Katowice, Poland*

Abstract

Data on $\bar{p}p$ annihilation in flight into $\pi^0\pi^0\eta$ are presented for nine beam momenta 600 to 1940 MeV/c. The strongest four intermediate states are found to be $f_2(1270)\eta$, $a_2(1320)\pi$, $\sigma\eta$ and $a_0(980)\pi$. Partial wave analysis is performed mainly to look for resonances formed by $\bar{p}p$ and decaying into $\pi^0\pi^0\eta$ through these intermediate states. There is evidence for the following s -channel $I = 0$ resonances : two 4^{++} resonances with mass and width (M, Γ) at (2044, 208) MeV and (2320 \pm 30, 220 \pm 30) MeV; three 2^{++} resonances at (2020 \pm 50, 200 \pm 70) MeV, (2240 \pm 40, 170 \pm 50) MeV and (2370 \pm 50, 320 \pm 50) MeV; two 3^{++} resonances at (2000 \pm 40, 250 \pm 40) MeV and (2280 \pm 30, 210 \pm 30) MeV; a 1^{++} resonance at (2340 \pm 40, 340 \pm 40) MeV; and two 2^{-+} resonances at (2040 \pm 40, 190 \pm 40) MeV and (2300 \pm 40, 270 \pm 40) MeV.

PACS: 13.75Cs, 14.20GK, 14.40

Keywords: mesons, resonances, annihilation

1 Introduction

The Crystal Barrel detector is being used to make a systematic study of the mass region 1960 to 2410 MeV in $\bar{p}p$ annihilation in flight at LEAR, with \bar{p} beams of momenta 600 to 1940 MeV/c. The objective is to study resonances in the formation process, i.e. the s -channel. Here we study data in $\bar{p}p \rightarrow \pi^0\pi^0\eta$ for resonances decaying to $a_2(1320)\pi^0$, $f_2(1270)\eta$, $f_0(1500)\eta$, $f_0(980)\eta$, $a_0(980)\pi^0$ and $\sigma\eta$. We use σ to denote the broad $\pi\pi$ S-wave amplitude up to ~ 1860 MeV. The present results have been presented briefly in the form of a letter [1] and here we give full details of the experimental techniques and analysis. Further studies of $\eta\eta\pi^0$ have been presented elsewhere [2,3], and work is in progress on other channels such as $3\pi^0$ and $\pi^0\pi^0\eta'$.

From earlier work, it is known that the mass range we explore contains many resonances [4]; a detailed study of $\bar{p}p \rightarrow \pi^-\pi^+$ using a polarised target has provided much of the current evidence [5,6]. The $f_4(2050)$ is well known, and from the quark model of meson resonances one expects that it will be accompanied by f_3 and f_2 resonances close-by in mass. We shall indeed provide evidence for these resonances and a further one with quantum numbers $J^{PC} = 2^{-+}$ and similar mass. At higher masses, towards the top of the LEAR range, there has been evidence for $f_4(2300)$ and $f_2(2340)$ [4], and it is anticipated from the Veneziano model [7] that there is likely to be a tower of resonances around this mass. We shall provide evidence for such states with quantum numbers 4^+ , 3^+ , 2^+ , 1^+ and 2^- .

These resonances are anticipated $\bar{q}q$ states. This mass range is also likely to contain glueballs with quantum numbers 0^{-+} and 2^{++} , predicted in the mass range 2000–2400 MeV by various theoretical models [8,9,10]. Hybrids may also be present. Decays of these exotic resonances to η and σ seem to be favoured in $f_0(1500)$ decay [11], charmonium decay and J/Ψ radiative decays [12]. Hence the $\eta f_2(1270)$ and $\eta\sigma$ channels are of particular interest.

The layout of this paper will be as follows. In section 2, the procedure for data processing and event selection is outlined; the data are presented and their gross features are discussed. Section 3 gives the formalism used for the partial wave analysis. Section 4 gives the results for partial wave amplitudes. Then, in Section 5 we fit partial waves to resonances. Finally, Section 6 provides a summary.

¹Now at IHEP, Beijing 100039, China

2 Experiment and Data Processing

The data were taken at LEAR by the Crystal Barrel Collaboration, using a trigger on neutral final states at nine beam momenta from 600 to 1940 MeV/c. An average of 9×10^6 triggers were taken at each momentum. The detector has been described fully in an earlier publication [13].

A liquid hydrogen target 4.4 cm long is surrounded at increasing radii by a silicon vertex detector, a multiwire chamber for triggering, a jet drift chamber to detect charged particles and finally 1380 CsI crystals to detect photons. The present data were taken with a trigger demanding a neutral final state. For this purpose, the silicon vertex detector, multiwire chamber and jet drift chamber were used simply to veto charged particles.

The barrel of CsI crystals covers 98% of 4π solid angle. Crystals are 16 radiation lengths long and point towards the target. The angular resolution is $\sim \pm 20$ mrad in both polar angle and azimuth. The detection efficiency is high for photons down to energies below 20 MeV. The energy resolution ΔE is given by $\Delta E/E = 0.025/E^{1/4}$, where E is in GeV.

The incident \bar{p} beam was pure and monoenergetic with momentum spread $\Delta p/p < 0.1\%$. Incident antiprotons were defined by a coincidence between a small proportional counter P and a 5mm diameter silicon counter, Si. Two veto counters, 20 cm downstream of the hydrogen target, were used to provide a first level trigger $P.Si.\bar{V}$ identifying interactions in the target. The beam intensity was typically $2 \times 10^5 \bar{p}/s$ and at times was twice this. The interaction rate in the target (excluding $\bar{p}p$ elastic scattering, where the forward \bar{p} generally counted in the veto counter) was typically 3KHz. Of this, $\sim 1 - 2\%$ consisted of neutral final states, so the trigger rate for all-neutral events was 20–60 Hz. In order to filter out events which obviously fail to conserve energy, the total energy in the CsI crystals was summed on-line [14]; a fast trigger rejected those events with total energy falling ~ 200 MeV or more below that of $\bar{p}p$ annihilation.

The absolute normalisation is derived from beam counts $P.Si$, target length and density, the number of detected events and a Monte Carlo simulation of reconstruction efficiency in the CsI barrel. Details of this normalisation are given in a paper on the $\pi^0\pi^0$ final state [15]. A dependence of the reconstruction efficiency on beam rate is observed, and the normalisation has to be obtained from an extrapolation to zero beam rate. The normalisation uncertainty is estimated as $\pm 3\%$ from 1800 to 1050 MeV/c and increases to $\pm 6\%$ at 900 and 600 MeV/c. Data at 1940 MeV/c were taken in separate, earlier runs, and have an estimated uncertainty of $\pm 10\%$ in normalisation. There is in addition an overall normalisation uncertainty of $\pm 2.4\%$ from the target length, common to all momenta.

2.1 Data Selection

A large number of alternative prescriptions have been examined for selecting events. At high momenta, one of the problems is that photons from π^0 decay sometimes merge into a single shower. Conversely, one shower sometimes splits into a primary shower and a nearby secondary shower, caused by Compton scattering. The probability that this occurs is $\sim 10\%$ per photon. In early studies, an attempt was made to salvage $\eta\pi^0\pi^0$ events from 5γ or 7γ final states. However, the gain in statistics was small ($\sim 15\%$) and the penalty was an increase in backgrounds. Eventually, it was decided to retain only events containing exactly 6 photon showers.

Beam Momentum (MeV/c)	Number of Events	Reconstruction Efficiency (%)	Cross Section (μb)
600	20385	26.3	71.9 ± 3.6
900	112476	25.4	83.2 ± 4.9
1050	86238	24.9	78.9 ± 2.3
1200	124581	24.2	68.6 ± 3.0
1350	81454	23.4	54.4 ± 2.3
1525	57714	22.7	56.5 ± 1.8
1642	65984	21.9	53.2 ± 2.5
1800	71738	20.8	43.8 ± 1.5
1940	75325	19.8	37.0 ± 3.7

Table 1: Numbers of selected events, reconstruction efficiency and cross sections for $\bar{p}p \rightarrow \pi^0\pi^0\eta$ with $\eta \rightarrow \gamma\gamma$.

Data are fitted kinematically to a large number of physics channels: 43 for $(4 - 8)\gamma$. In order to assess branching ratios to every channel and cross-talk between them, we generate at least 20,000 Monte Carlo events for every one of the 43 fitted channels, using GEANT. In the first approximation, events fitting the correct channel determine the reconstruction efficiency ϵ_i in each channel. Events fitting the wrong channel estimate the probability of cross-talk x_{ij} between channels i and j . More exactly, we solve a set of 43 x 43 simultaneous equations containing on the left-hand side the observed number of fitted data events D_i , and on the right-hand side reconstruction efficiencies and true numbers of created events N_i in every channel and terms allowing for cross-talk x_{ij} between channels:

$$D_i = \epsilon_i N_i + \sum_{j \neq i} x_{ij} N_j. \quad (1)$$

The solution is constrained so that the numbers of real events, N_i , in every channel are positive or zero.

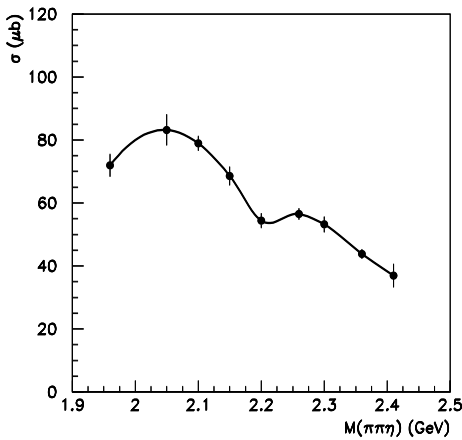


Figure 1: Cross section for $\bar{p}p \rightarrow \pi^0\pi^0\eta$ with $\eta \rightarrow \gamma\gamma$.

This procedure is carried out for a variety of confidence levels (1, 5, 10, 20%) and using a wide variety of selection procedures. A choice is then made, optimising the ratio of signal to background. We find that this ratio is not very sensitive to confidence level over the range 5–20% for $\eta\pi^0\pi^0$ events.

Among 6 – 8 photon events, the four largest channels are $4\pi^0$, $3\pi^0$, $\pi^0\pi^0\eta$ and $\pi^0\pi^0\omega$ with $\omega \rightarrow \pi^0\gamma$. The relative branching ratios for these channels are roughly 1.1 : 1 : 0.4 : 0.4 at 1800 MeV/c. To select the $\pi^0\pi^0\eta$ channel, we demand exactly 6 photons satisfying a 7C kinematic fit with confidence level > 10%; events fitting $3\pi^0$ with confidence level > 0.01% are rejected, and also those few events fitting $\pi^0\pi^0\eta'$, $\pi^0\eta\eta'$, $\pi^0\eta\eta'$ and 3η with confidence level larger than that for $\pi^0\pi^0\eta$. The Monte Carlo simulation shows that the worst backgrounds arise from $\omega\pi^0\pi^0$, ($\omega \rightarrow \pi^0\gamma$) when one photon is lost, and from $4\pi^0$ events when two photons are lost. Residual backgrounds from these two processes are 1.5% and 0.8% respectively at 1800 MeV/c. Including other small backgrounds, the total is $3.0 \pm 0.3\%$ at 1800 MeV/c. For lower beam momenta, the background increases slightly. At 600 MeV, the total is 4.0 ± 0.4 with the worst backgrounds from $\omega\pi^0\pi^0$ (1.7%), $4\pi^0$ (0.9%) and $\omega\omega$ (0.9%). Table 1 summarises numbers of selected events, the reconstruction efficiency and cross sections. Statistics at 600 MeV/c are lower because most data were taken without the threshold cut on total energy in the trigger. The cross sections for the $\eta\pi^0\pi^0$ channel are also shown in Fig.1. There are clear enhancements at low mass and around 2200–2300 MeV. Note that for a constant amplitude the cross sections should decrease steadily as the energy increases, see equn (23) below.

Fig. 2 shows the confidence level (CL) distribution for data of beam momentum at 1.2 GeV/c. The slight peak at high confidence level arises from events where all particles emerge close to the beam direction, with the result that the vertex is poorly defined. We apply no cut on the coordinate of the vertex along the beam direction, so as to avoid biasing the data selection. The rise at low confidence levels is followed accurately down to 10% by the Monte Carlo simulation; it arises from overlapping showers in the CsI detectors.

In order to illustrate the cleanliness of the η signal, we have made an additional fit to $\pi^0\pi^0\gamma\gamma$. Fig. 3 then shows the mass distribution of $\gamma\gamma$ pairs in the vicinity of the η peak for $CL(\pi^0\pi^0\gamma\gamma) > 0.1$ with $CL(\pi^0\pi^0\eta) > 0.0001$ at beam momentum 1.2 GeV/c. The η peak is well centred at the correct mass, 547.5 MeV and the background under the η signal is compatible with that expected from the Monte Carlo simulation.

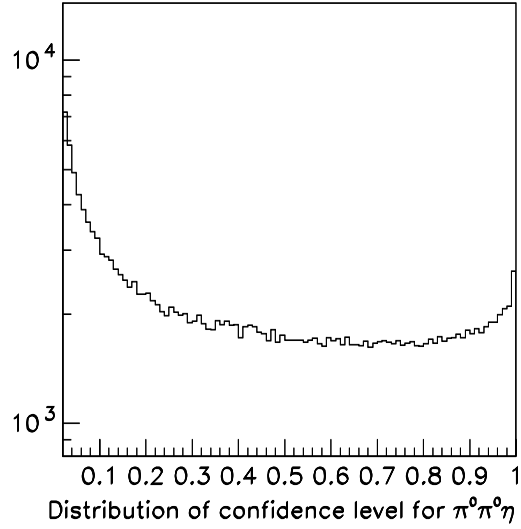


Figure 2: Distribution of confidence level for $\bar{p}p \rightarrow \pi^0\pi^0\eta$ events at beam momentum 1.2 GeV/c.

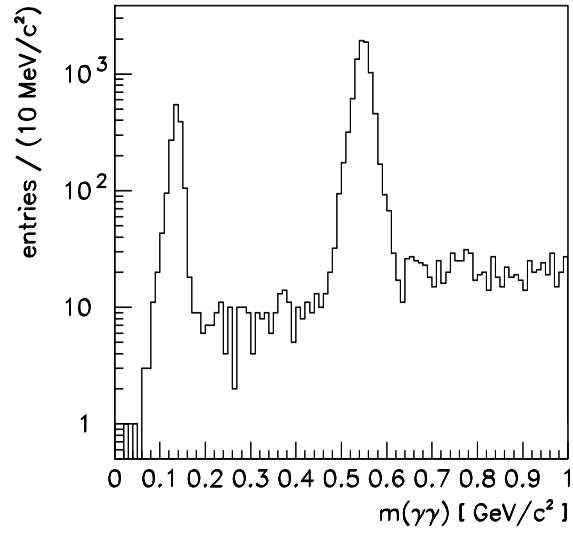


Figure 3: Mass distribution of $\gamma\gamma$ pairs for $CL(\pi^0\pi^0\gamma\gamma) > 0.1$ with $CL(\pi^0\pi^0\eta) > 0.0001$ at beam momentum 1.2 GeV/c.

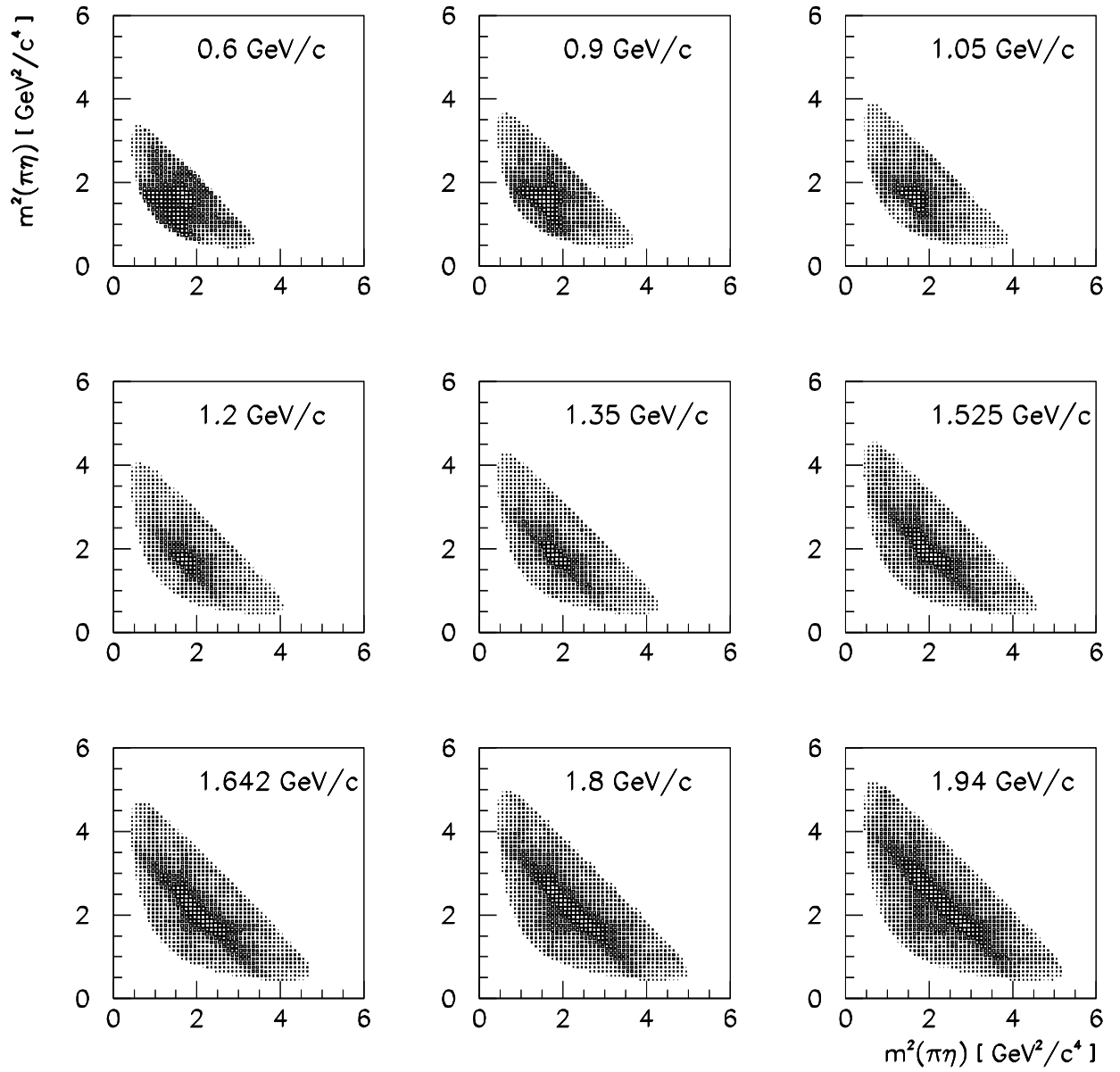


Figure 4: Dalitz plots for $\bar{p}p \rightarrow \pi^0\pi^0\eta$ at incident beam momenta 0.6 – 1.94 GeV/c.

2.2 Features of the Data

Fig. 4 shows Dalitz plots at the nine available momenta and Figs. 5 and 6 projections on to $\eta\pi$ mass and $\pi\pi$ mass. The most prominent feature of the Dalitz plot consists of a diagonal band due to $f_2(1270)\pi^0$. There are weaker horizontal and vertical bands due to $a_0(980)\pi$ and $a_2(1320)\pi$. The $f_2(1270)\eta$ signal grows with respect to $a_2(1320)\pi$ as the beam momentum rises; this is a natural consequence of the increasing phase space for $f_2(1270)\eta$, whose threshold is at 1820 MeV. Very weak peaks are visible in the $\pi\pi$ mass projection of Fig. 6 due to $f_0(1500)\eta$ and $f_0(980)\eta$. In addition, there is some slowly varying contribution covering the whole Dalitz plots; it may come from the broad σ , i.e., $f_0(400-1200)$ in the Particle Data Tables [4]. We adjust fitted masses and widths of $f_2(1270)$ and $a_2(1320)$ by a few MeV from PDG values in order to achieve the optimum fits. This is because our main aim is to fit the production and decay angular distributions of these resonances.

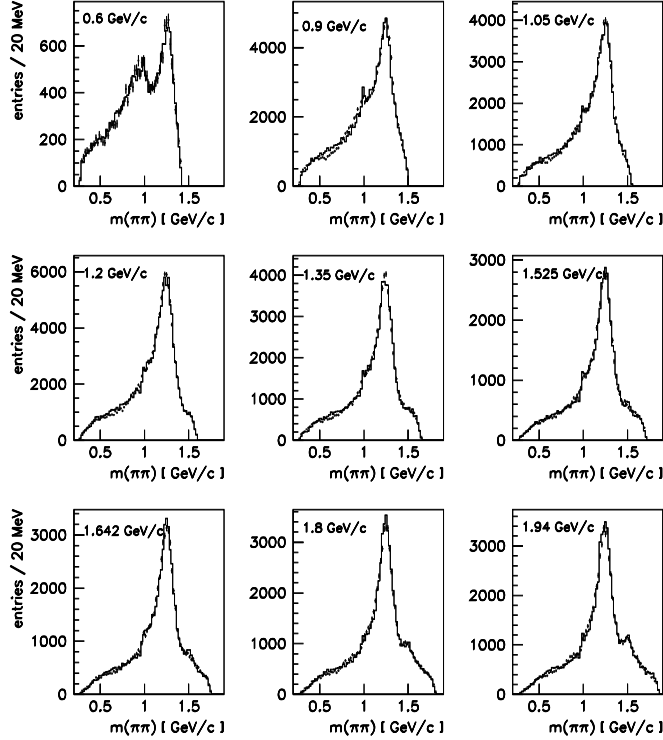


Figure 5: Data and fit (histogram) of invariant mass spectra for $\pi^0\pi^0$ (1 entry/event).

Figs. 7 and 8 show differences on the Dalitz plot between fit and data. There are small systematic discrepancies at the extreme right-hand edge of the Dalitz plot near an $\eta\pi$ mass of 1450 MeV. This discrepancy may be due to $a_0(1450)$ or $a_2(1660)$ or $\rho(1405)$. The effect is small and cannot be analysed unambiguously into partial waves. Fits including these components have almost no effect on the main components of the fit, with the exception of $\eta\sigma$, which covers the whole Dalitz plot and can absorb other small, ill-defined contributions.

Figs. 9 and 10 show production angular distributions (after acceptance correction) for events lying in the $f_2(1270)$ mass band (1275 ± 100 MeV) and for events lying in the $a_2(1320)$ mass band (1320 ± 50 MeV). It is immediately obvious that high orbital angular momenta are involved for both $f_2\eta$ and $a_2\pi$ at the higher beam momenta. The histograms show results of the partial wave fit described below.

3 Formalism for Partial Wave Analysis

For the $\pi^0\pi^0\eta$ final state, possible $\bar{p}p$ initial singlet states are 0^{-+} , 2^{-+} , 4^{-+} etc; for $\bar{p}p$ spin triplet, allowed states are 1^{++} , 2^{++} , 3^{++} , 4^{++} , 5^{++} etc. For our case with center-of-mass energies below 2.41 GeV, only 0^{-+} ,

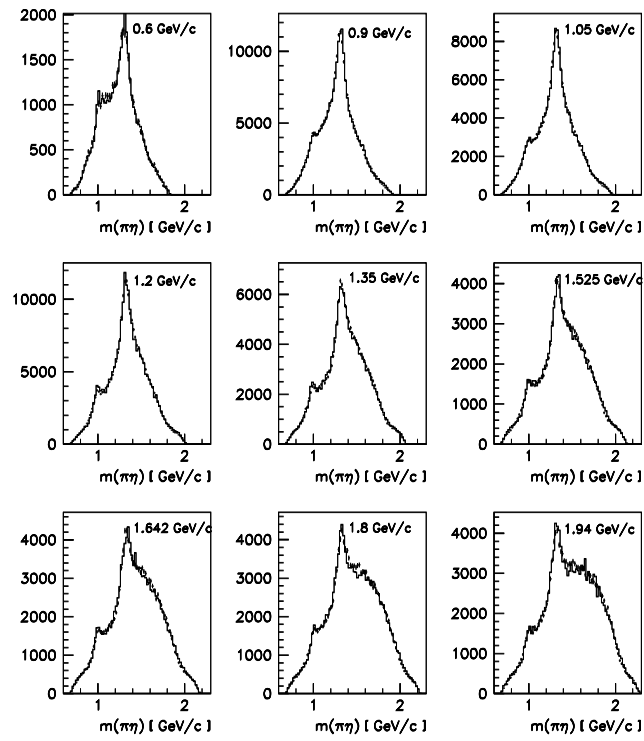


Figure 6: Data and fit (histogram) of invariant mass spectra for $\pi^0\eta$ (2 entries/event).

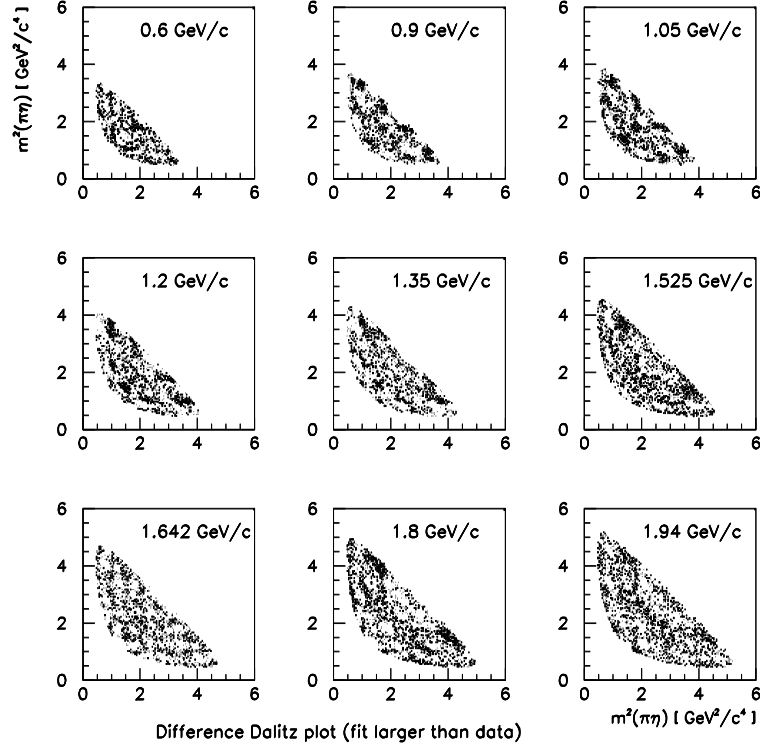


Figure 7: Difference between Dalitz plots of fit and data where fit > data.

2^{-+} , 1^{++} , 2^{++} , 3^{++} and 4^{++} are expected to be significant [6] and this has been confirmed in our analysis; 4^{-+} has been tried, but is not significant. The corresponding $\bar{p}p$ states with total angular momentum J , orbital angular momentum L and total spin angular momentum S in the usual contracted form $^{2S+1}L_J$ are: 1S_0 for 0^{-+} , 1D_2 for 2^{-+} , 3P_1 for 1^{++} , 3P_2 or 3F_2 for 2^{++} , 3F_3 for 3^{++} , and 3F_4 or 3H_4 for 4^{++} .

Let us choose the reaction rest frame with the z axis along the \bar{p} beam direction. Then the squared modulus of the total transition amplitude is the following [16]:

$$\begin{aligned}
I &= |A_{0^{-+}} + A_{2^{-+}}|^2 + |A_{1^{++}}^{M=1} + A_{3^{++}}^{M=1}|^2 + |A_{1^{++}}^{M=-1} + A_{3^{++}}^{M=-1}|^2 \\
&+ |A_{2^{++}}^{M=0} + A_{4^{++}}^{M=0}|^2 + |A_{2^{++}}^{M=1} + A_{4^{++}}^{M=1}|^2 + |A_{2^{++}}^{M=-1} + A_{4^{++}}^{M=-1}|^2 \\
&+ 2\text{Re}[(A_{2^{++}}^{M=1} + A_{4^{++}}^{M=1})(A_{1^{++}}^{M=1} + A_{3^{++}}^{M=1})^* - (A_{2^{++}}^{M=-1} + A_{4^{++}}^{M=-1})(A_{1^{++}}^{M=-1} + A_{3^{++}}^{M=-1})^*]
\end{aligned} \tag{2}$$

where M is the spin projection on the z -axis in the initial state. The absence of $M=0$ for 1^{++} and 3^{++} is due to the vanishing of the Clebsch-Gordon (CG) coefficient ($J = 2n + 1, M_J = 0 | L = 2n + 1, M_L = 0; S = 1, M_S = 0$) with n as an integer. The relative minus sign for the interference term of (*even*) $^{++}$ and (*odd*) $^{++}$ partial waves with $M=1$ and $M=-1$ is also due to a property of CG coefficients.

Each partial wave amplitude A_{JPC} includes contributions from various intermediate states (n), i.e.,

$$A_{JPC} = \sum_n C_n A_{JPC \rightarrow n} \tag{3}$$

where C_n are free complex parameters to fit the data. In the present analysis, only $f_2(1270)\eta$, $a_2(1320)\pi$, $a_0(980)\pi$, $\sigma\eta$, $f_0(980)\eta$ and $f_0(1500)\eta$ intermediate states are considered. Amplitudes $A_{JPC \rightarrow n}$ are constructed from relativistic Lorentz covariant tensors, Breit-Wigner functions and Blatt-Weisskopf barrier factors [17]. The amplitudes used for $f_0(1500)\eta$ and $f_2(1270)\eta$ intermediate states in our final fit are the following:

$$A_{0^{-+} \rightarrow f_0\eta} = G_{f_0}, \tag{4}$$

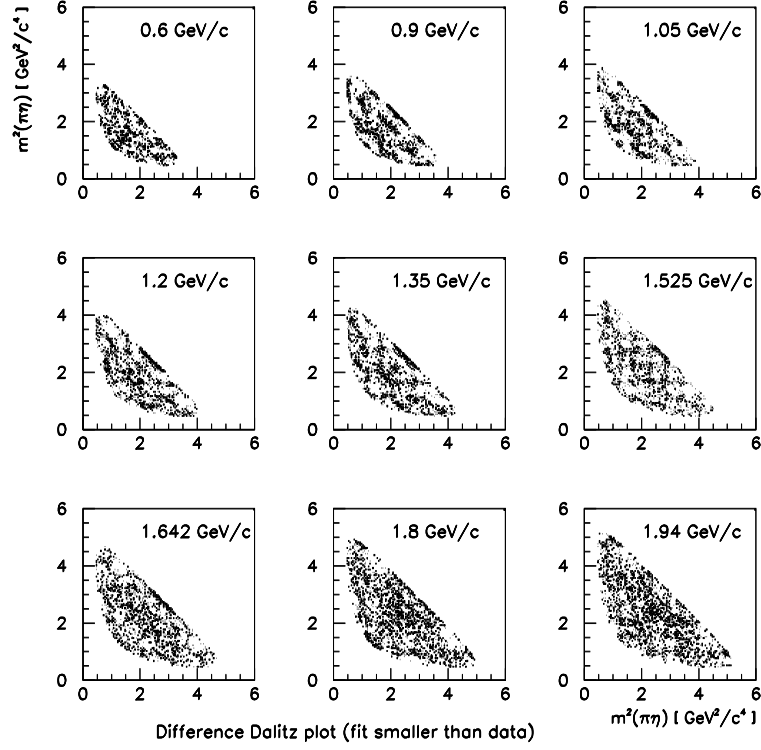


Figure 8: Difference between Dalitz plots of fit and data where fit < data.

$$A_{0^{-+} \rightarrow f_2 \eta} = T^{\alpha\beta} \tilde{t}_{\alpha\beta}^{(2)} B_2(k) G_{f_2}, \quad (5)$$

$$A_{2^{-+} \rightarrow f_0 \eta} = \phi^{\alpha\beta}(0) \tilde{t}_{\alpha\beta}^{(2)} B_2(k) G_{f_0}, \quad (6)$$

$$A_{2^{-+} \rightarrow f_2 \eta (l=0)} = \phi^{\alpha\beta}(0) T_{\alpha\beta} G_{f_2}, \quad (7)$$

$$A_{2^{-+} \rightarrow f_2 \eta (l=2)} = \phi^{\alpha\beta}(0) \tilde{t}_{\alpha\gamma}^{(2)} T_{\beta}^{\gamma} B_2(k) G_{f_2}, \quad (8)$$

$$A_{1^{++} \rightarrow f_0 \eta}^M = \phi^{\alpha}(M) \tilde{t}_{\alpha}^{(1)} B_1(k) G_{f_0}, \quad (9)$$

$$A_{1^{++} \rightarrow f_2 \eta (l=1)}^M = \phi_{\alpha}(M) \tilde{t}_{\beta}^{(1)} T^{\alpha\beta} B_1(k) G_{f_2}, \quad (10)$$

$$A_{1^{++} \rightarrow f_2 \eta (l=3)}^M = \phi^{\alpha}(M) \tilde{t}_{\alpha\beta\gamma}^{(3)} T^{\beta\gamma} B_3(k) G_{f_2}, \quad (11)$$

$$A_{2^{++} \rightarrow f_2 \eta (l=1)}^M = \phi_{\mu\alpha}(M) \epsilon^{\alpha\beta\gamma\delta} P_{\beta} \tilde{t}_{\gamma}^{(1)} T_{\delta}^{\mu} B_1(k) G_{f_2}, \quad (12)$$

$$A_{2^{++} \rightarrow f_2 \eta (l=3)}^M = \phi_{\mu\alpha}(M) \epsilon^{\alpha\beta\gamma\delta} P_{\beta} \tilde{t}_{\gamma}^{(3)\mu\nu} T_{\delta}^{\nu} B_3(k) G_{f_2}, \quad (13)$$

$$A_{3^{++} \rightarrow f_0 \eta}^M = \phi^{\alpha\beta\gamma}(M) k_{\alpha} k_{\beta} k_{\gamma} B_3(k) G_{f_0}, \quad (14)$$

$$A_{3^{++} \rightarrow f_2 \eta (l=1)}^M = \phi^{\alpha\beta\gamma}(M) \tilde{t}_{\alpha}^{(1)} T_{\beta\gamma} B_1(k) G_{f_2}, \quad (15)$$

$$A_{3^{++} \rightarrow f_2 \eta (l=3)}^M = \phi^{\alpha\beta\gamma}(M) \tilde{t}_{\alpha\beta\delta}^{(3)} T_{\gamma}^{\delta} B_3(k) G_{f_2}, \quad (16)$$

$$A_{4^{++} \rightarrow f_2 \eta (l=3)}^M = \phi^{\mu\nu\lambda\alpha}(M) k_{\mu} k_{\nu} \epsilon_{\alpha\beta\gamma\delta} P^{\beta} k^{\gamma} T_{\lambda}^{\delta} B_3(k) G_{f_2} \quad (17)$$

where k_{μ} is the four-momentum of the η , $G_{f_0} = (M_{f_0}^2 - s_{\pi\pi} - iM_{f_0}\Gamma_{f_0})^{-1}$ and $G_{f_2} = (M_{f_2}^2 - s_{\pi\pi} - iM_{f_2}\Gamma_{f_2})^{-1}$ are Breit-Wigner propagators for f_0 and f_2 . $T_{\mu\nu}$ is a rank-2 tensor for f_2 and is formed by the four-momentum (p) of f_2 and its break-up four-momentum (q) as

$$T_{\mu\nu} = [q_{\mu}q_{\nu} - \frac{1}{3}(g_{\mu\nu} - \frac{p_{\mu}p_{\nu}}{s_{\pi\pi}})q^2]B_2(q). \quad (18)$$

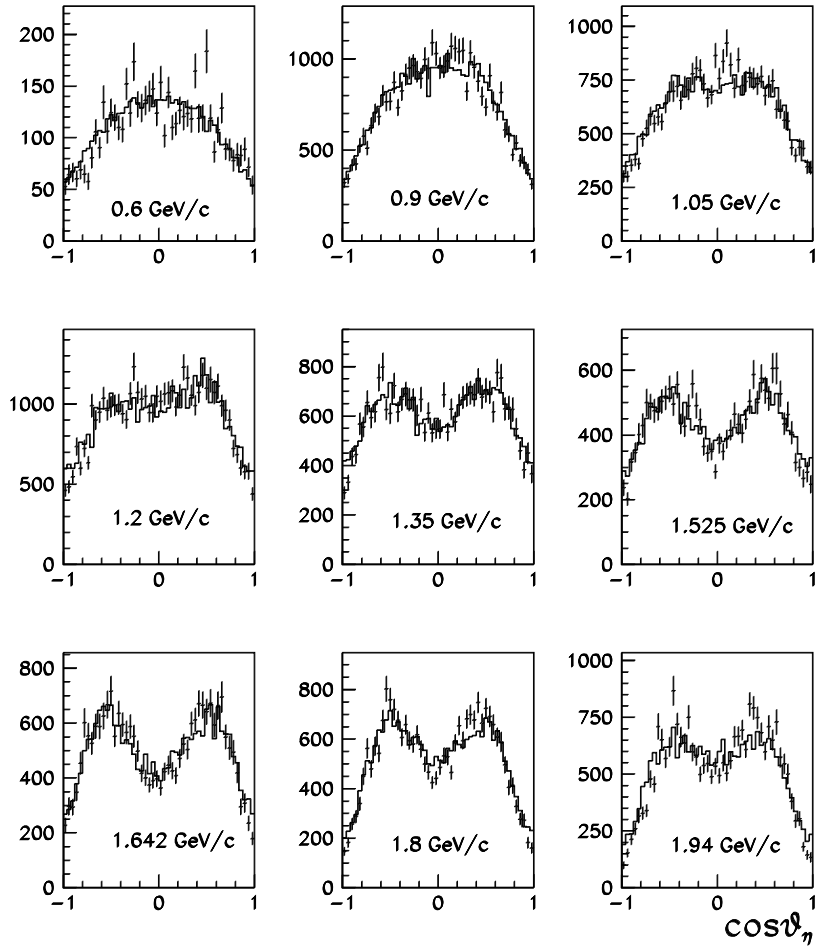


Figure 9: Data and fit (histogram) of angular distribution $d\sigma/d \cos\theta_\eta$ for $M_{\pi\pi}$ between 1175 and 1375 MeV (1 entry/event).

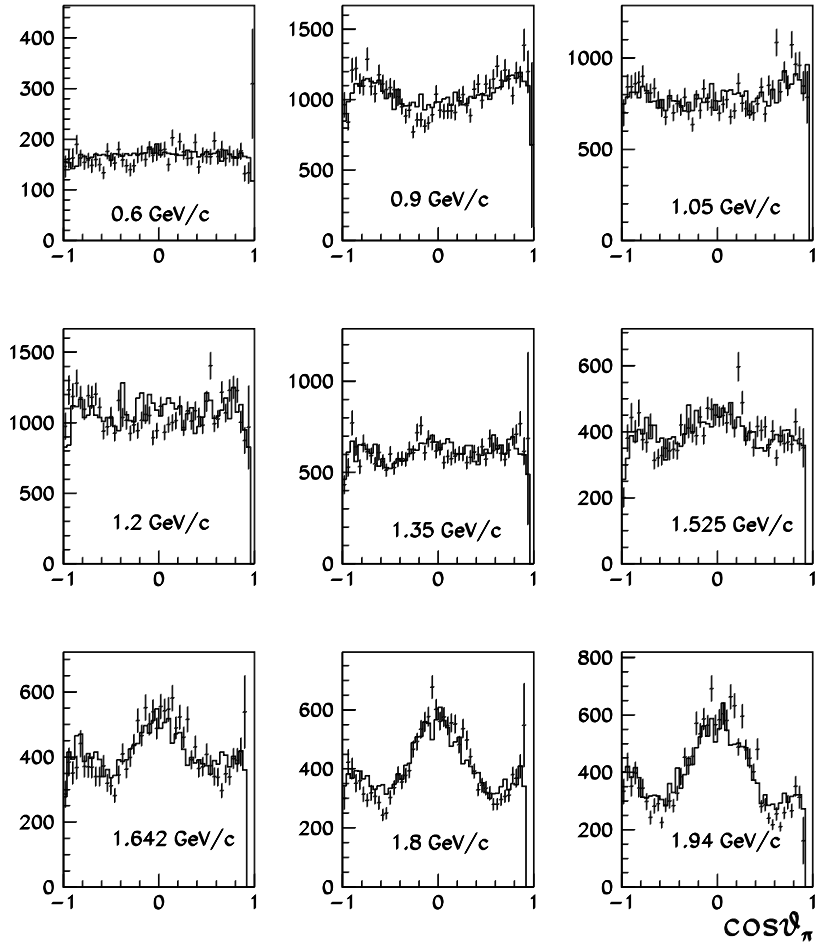


Figure 10: Data and fit (histogram) of angular distribution $d\sigma/d \cos\theta_\pi$ for $M_{\eta\pi}$ between 1270 and 1370 MeV (2 entries/event).

The Blatt-Weisskopf barrier factors $B_l(k)$ with a radius of 1 fm, the rank- l tensors $\hat{t}_{\delta_1 \dots \delta_l}^{(l)}$ for pure l -wave orbital angular momentum of the $\eta f_{0,2}$ system, and the spin- J wave functions $\phi^{\delta_1 \dots \delta_J}(M)$ are standard as given in [17].

For $f_0(980)\eta$ and $\sigma\eta$ intermediate states, the formulae are the same as for $f_0(1500)\eta$ except for a different G_{f_0} for which we take the parameterization of Ref. [18], i.e.,

$$G_{f_0(980)} = \frac{1}{M_R^2 - s_{\pi\pi} - ig_\pi \sqrt{1 - 4m_\pi^2/s_{\pi\pi}} - ig_K \sqrt{1 - 4m_K^2/s_{\pi\pi}}} \quad (19)$$

with $M_R = 0.99$ GeV, $g_\pi = 0.117$ GeV², $g_K = 0.273$ GeV², $m_\pi = 0.135$ GeV and $m_K = 0.496$ GeV;

$$G_\sigma = \frac{1 + C_0 s_{\pi\pi}}{M_\sigma^2 - s_{\pi\pi} - iM_\sigma(\Gamma_1(s_{\pi\pi}) + \Gamma_2(s_{\pi\pi}))}, \quad (20)$$

where C_0 is a complex constant to be fitted by the data,

$$\Gamma_1(s) = G_1 \frac{\sqrt{1 - 4m_\pi^2/s}}{\sqrt{1 - 4m_\pi^2/M_\sigma^2}} \cdot \frac{(s - m_\pi^2/2)}{(M_\sigma^2 - m_\pi^2/2)} e^{-(s - M_\sigma^2)/4\beta^2} \quad (21)$$

$$\Gamma_2(s) = G_2 \frac{\sqrt{1 - 16m_\pi^2/s}}{1 + \exp(\Lambda(s_0 - s))} \cdot \frac{1 + \exp(\Lambda(s_0 - M_\sigma^2))}{\sqrt{1 - 16m_\pi^2/M_\sigma^2}} \quad (22)$$

with $M_\sigma = 1.067$ GeV, $G_1 = 1.378$ GeV, $\beta = 0.7$ GeV, $G_2 = 0.0036$ GeV, $\Lambda = 3.5$ GeV⁻² and $s_0 = 2.8$ GeV².

For $a_0\pi$ and $a_2\pi$ intermediate states, the formulae are similar to those for $f_0\eta$ and $f_2\eta$, but need symmetrization for two pions. The Breit-Wigner propagators for a_0 , a_2 , $f_0(1500)$ and f_2 assume constant widths. The masses and widths (M , Γ) for a_0 and $f_0(1500)$ are fixed to be (0.9834, 0.085) GeV and (1.495, 120), respectively. Those for a_2 and f_2 are adjusted to fit the data. Based on these formulae, the data at each momentum are fitted by the maximum likelihood method.

It is possible that the process $\bar{p}p \rightarrow \eta\pi^0\pi^0$ is driven, at least partially, by t -channel Regge exchanges. Even so, by Watson's theorem, each partial wave will acquire the phase variation of any s -channel resonance which is present; that is, amplitudes will contain singularities due to both s - and t -channel poles. Our strategy will be to express T matrices for individual partial waves $T_{L,J}$ as sums over s -channel resonances. The formulae we use are

$$\sigma_{JPC \rightarrow n}(s) = N \frac{k_n}{s k_i} |A_{JPC \rightarrow n}(s)|^2, \quad (23)$$

$$A_{JPC \rightarrow n}(s) = \sum_j \frac{B_L(k_i) \Lambda_{nj} B_l(k_n)}{M_{nj}^2 - s - iM_{nj} \Gamma_{nj}}, \quad (24)$$

where $s = M_{\bar{p}p}^2 = M_{\pi\pi\eta}^2$, N is the normalization constant, k_i and k_n are the center-of-mass momenta of initial state and channel n respectively; B_L and B_l are barrier factors for the initial state and state n respectively; Λ_{nj} are complex fitting parameters; M_{nj} and Γ_{nj} are masses and widths for resonances to be fitted. This prescription builds in the required threshold behaviour in each partial wave. By using a sum of resonances, we satisfy the constraint of analyticity.

4 Results for partial waves

The fit is shown as histograms in Figs. 5-6 for the mass spectra. It is obviously not perfect as regards broad, slowly varying components in the $\pi\pi$ projection of Fig. 6. However, since we are mainly interested in scanning the larger components from $f_2(1270)\eta$, $\sigma\eta$, $a_2\pi$ and $a_0(980)\pi$ intermediate states, we ignore those smaller contributions for the present study.

The intensities of dominant partial waves are displayed in Fig. 11, and we shall discuss a fit to them below. The data points with error bars shown in Figs. 11 and 12 are our final fitted results for the partial wave cross sections $\sigma_{JPC \rightarrow n}$ at each momentum for $\bar{p}p \rightarrow \pi^0\pi^0\eta$ with $\eta \rightarrow \gamma\gamma$. Small waves are displayed in Fig. 12. Partial waves with less significant contribution than those in Fig.12 are dropped from our final fit. Table 2 shows the

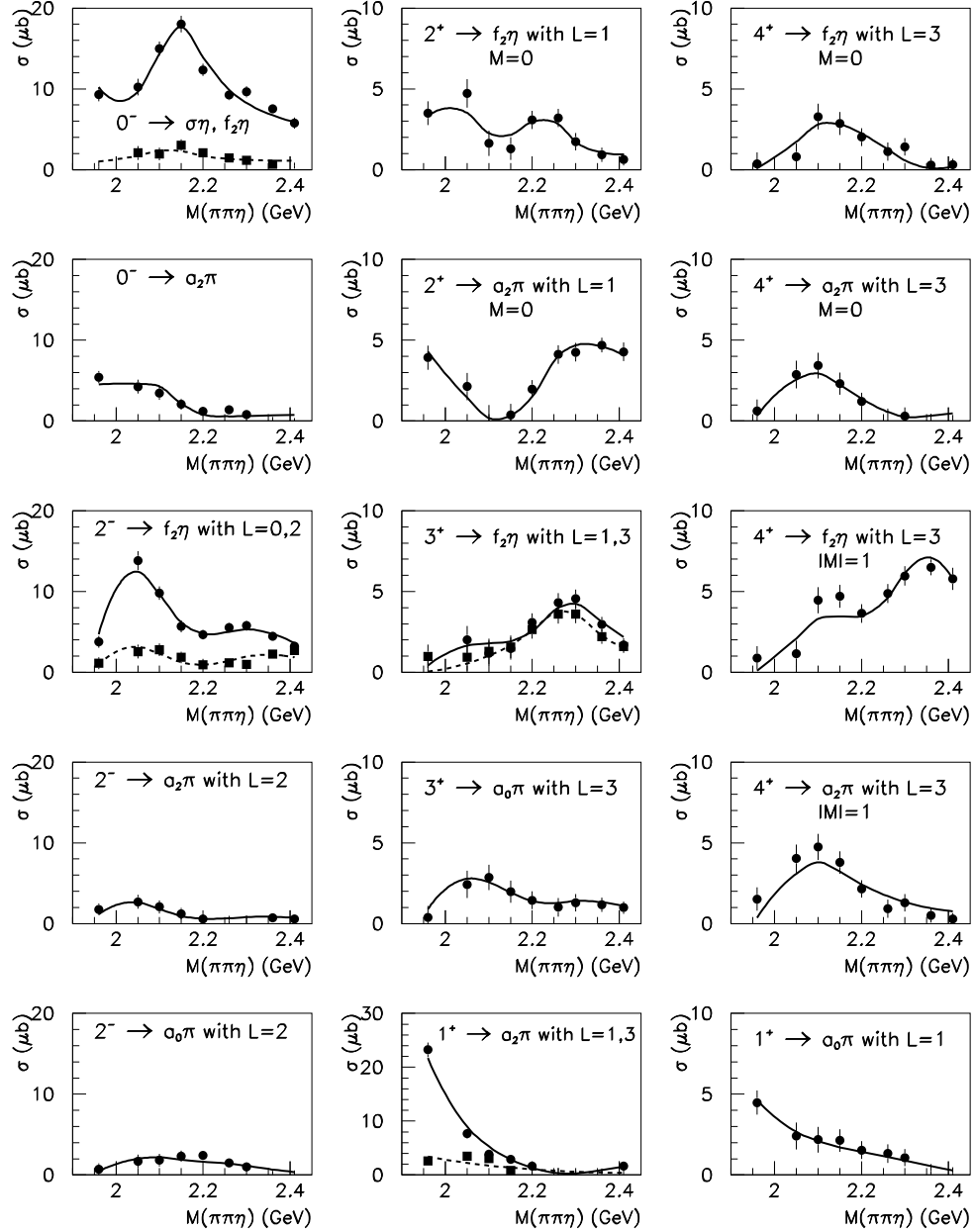


Figure 11: Cross sections for partial waves making the largest contributions to $\bar{p}p \rightarrow \pi^0 \pi^0 \eta$ with $\eta \rightarrow \gamma\gamma$. For diagrams with two components, the first label corresponds to the bigger component. The curves are the fit to the data points in the figure and the relative phases between components.

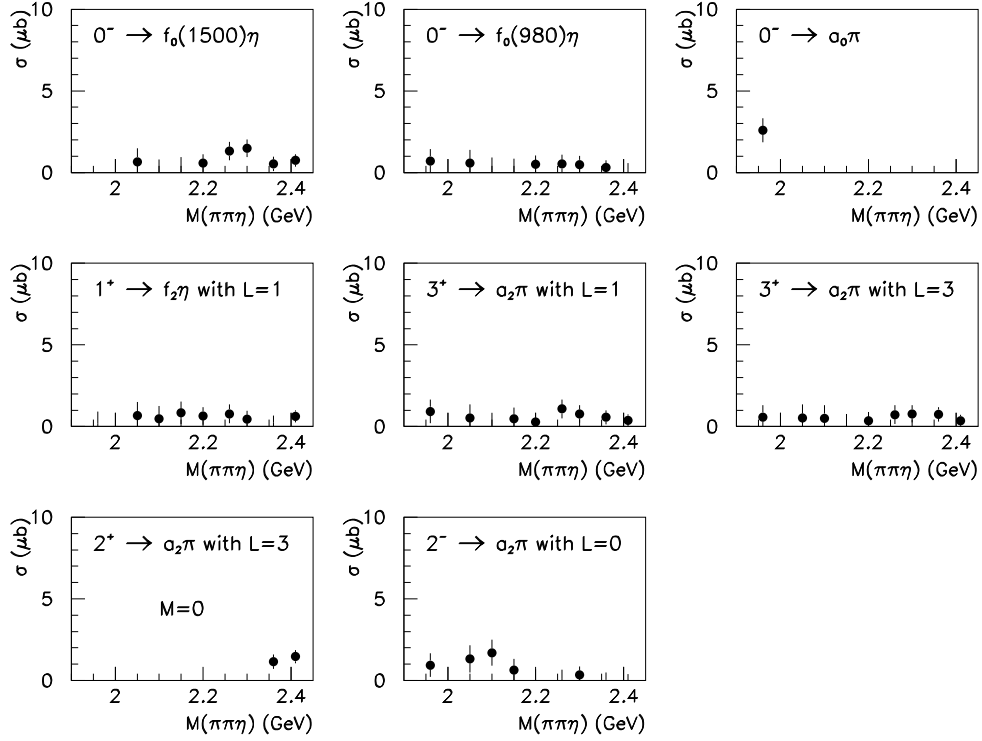


Figure 12: Cross sections for partial waves included in the final fit but giving smaller contributions than those in Fig. 11 to $\bar{p}p \rightarrow \pi^0 \pi^0 \eta$ with $\eta \rightarrow \gamma\gamma$.

J^{PC}	Mass (MeV)	Width (MeV)	$\frac{\Gamma_{\bar{p}p} \Gamma_{f_2 \eta}}{\Gamma_{tot}^2} \cdot 10^3$	$\frac{\Gamma_{\bar{p}p} \Gamma_{a_2 \pi}}{\Gamma_{tot}^2} \cdot 10^3$	$\frac{\Gamma_{\bar{p}p} \Gamma_{\sigma \eta}}{\Gamma_{tot}^2} \cdot 10^3$	$\frac{\Gamma_{\bar{p}p} \Gamma_{a_0 \pi}}{\Gamma_{tot}^2} \cdot 10^3$
4^{++}	2044	208	0.54 ± 0.14	5.1 ± 0.8	-	-
4^{++}	2320 ± 30	220 ± 30	1.3 ± 0.4	0.6 ± 0.6	-	-
3^{++}	2000 ± 40	250 ± 40	0.12 ± 0.08	0.6 ± 0.6	-	0.23 ± 0.11
3^{++}	2280 ± 30	210 ± 30	1.7 ± 0.4	4.5 ± 2.6	-	0.23 ± 0.19
2^{++}	2020 ± 50	200 ± 70	2.1 ± 0.4	4.3 ± 1.2	-	-
2^{++}	2240 ± 40	170 ± 50	2.5 ± 0.6	1.6 ± 1.6	-	-
2^{++}	2370 ± 50	320 ± 50	0.88 ± 0.64	16 ± 5	-	-
1^{++}	~ 1700	~ 270	-	-	-	-
1^{++}	2340 ± 40	340 ± 40	0.6 ± 0.6	60 ± 30	-	0.84 ± 0.53
0^{-+}	2140 ± 30	150 ± 30	1.9 ± 1.7	6 ± 6	10 ± 5	-
2^{-+}	2040 ± 40	190 ± 40	3.0 ± 0.3	5.0 ± 2.1	-	0.4 ± 0.2
2^{-+}	2300 ± 40	270 ± 40	2.8 ± 0.7	2.0 ± 2.0	-	0.5 ± 0.5

Table 2: Summary of fitted masses, widths and branching ratios corrected for their unseen decay modes. The mass and width of $f_4(2050)$ are fixed at PDG values, and the status of the 0^{-} state at 2140 MeV is questionable, as discussed in the text. The $f_1(1700)$ is beyond the accessible mass range. All states have $I = 0$, $G = +1$.

masses and widths of resonances included in the fit. Errors cover the range of values observed in a large variety of fits. The $f_1(1700)$ is below the range of masses accessible here, so its parameters are only approximate.

The relative phases of the partial waves at each momentum are shown in Fig.13. Since there is no interference between spin singlet and spin triplet, or between $M=0$ and $M=1$ for spin triplet, there will be one overall phase undetermined for each M of spin triplet and for spin singlet. Hence we can only determine relative phases from our partial wave analysis. For spin singlet (0^- and 2^-), the phases are relative to the partial wave of $2^- \rightarrow f_2\eta$ with $L=0$. For spin triplet with $M=0$, the phases are shown relative to $4^+ \rightarrow a_2\pi$ with $L=3$. For spin triplet with $|M|=1$, the phases are relative to $4^+ \rightarrow f_2\eta$ with $L=3$.

4.1 $J^P = 4^+$

For 4^{++} , a peak around 2090 MeV is clear for all 4^{++} channels. It can be fitted by a Breit-Wigner amplitude with the mass and width fixed to the PDG values for the well established 4^+ resonance $f_4(2050)$. The shift of the peak position to 2090 MeV is due to the centrifugal barrier factors for both initial and final states. Its decays into $f_2\eta$ and $a_2\pi$ appear with comparable strength in the $\eta\pi^0\pi^0$ channel.

In addition to the $f_4(2050)$, there is clearly another 4^{++} peak around 2.32 GeV in $4^+ \rightarrow f_2\eta$ in the $M=1$ partial wave. This resonance may be identified with $f_4(2300)$ of the PDG, observed earlier in many analyses of $\bar{p}p \rightarrow \pi^-\pi^+$. The mass, width and phase with respect to $f_4(2050)$ are adjusted freely. The mass optimises at $M = 2320 \pm 30$ MeV and the width at $\Gamma = 220 \pm 30$ MeV. These agree closely with earlier determination quoted by the PDG, and also with recent VES data on $\eta\pi^+\pi^-$ in the πA reaction [19]. The latter find $M = 2330 \pm 10(stat) \pm 20(syst)$ MeV, $\Gamma = 225 \pm 20 \pm 40$ MeV. They also observe this resonance in $\omega\omega$ data [20]. The $f_4(2300)$ is also observed in our data on $\bar{p}p \rightarrow \pi^0\pi^0$ [15], with a slightly lower mass of 2295 MeV. The $f_4(2300)$ resonance acts as a valuable interferometer, determining the phases of 3^+ , 2^+ and 1^+ amplitudes over the mass range 2150–2400 MeV.

From the $M = 1$ and $M = 0$ amplitudes for 4^+ , we reconstruct the linear combinations for 3F_4 and 3H_4 . Their intensities are shown in Fig. 14 for $f_2(1270)\eta$ and $a_2(1320)\pi$ channels. The $f_4(2050)$ resonance is almost purely 3F_4 . The $a_2\pi$ channel is fed mostly by $f_4(2050)$ with a possible weak contribution from $f_4(2320)$; the 3H_4 contribution to $a_2\pi$ is barely significant. In contrast, the $f_2\eta$ channel is fed by both $f_4(2050)$ and $f_4(2320)$ and the latter has a strong 3H_4 component. This is in agreement with the analysis of $\bar{p}p \rightarrow \pi^-\pi^+$ by Hasan and Bugg [6]; their Fig. 3 shows a strong 3H_4 component in $f_4(2320)$. The VES collaboration [19] finds that $f_4(2320)$ decays dominantly to $f_2\eta$, in agreement with present results.

4.2 $J^P = 3^+$

For $J^{PC} = 3^{++}$, there are significant enhancements at low mass ($M \simeq 2000$ MeV) in both $a_0(980)\pi$ and $f_2(1270)\eta$ with $L = 1$. At high mass ($M \simeq 2280$ MeV) there is a strong peak in $f_2(1270)\eta$ decays with both $L = 1$ and $L = 3$ decays. Fitted masses and widths are given in Table 2. There are no earlier listings of these resonances by the PDG. The observed phase with respect to $f_4(2050)$ and $f_4(2300)$ shown in Fig. 13 obviously requires the presence of at least one 3^+ resonance, and is poorly fitted without two. The Argand diagram is shown in fig. 15.

4.3 $J^P = 2^+$

For 2^{++} , there is a peak in $f_2(1270)\eta$ at ~ 2020 MeV and a peak at low masses in $a_2(1320)\pi$. At high mass around 2300 MeV, there is a strong peak in the $a_2(1320)\pi$ channel. In $f_2(1270)\eta$, there is a further peak at ~ 2230 MeV. The obvious question is how many resonances are required to fit these diverse structures. The phase variation observed on the Argand diagram, Fig. 15, requires at least two resonances from the observed 360° phase advance.

We find that the fit is poor without three resonances. The lowest peak fits naturally to a resonance with $M = 2020 \pm 50$ MeV, $\Gamma = 200 \pm 70$ MeV. Our data on $\bar{p}p \rightarrow \pi^0\pi^0$ independently find a resonance at 2020 MeV [15], and the analysis of Hasan and Bugg [6] of data on $\bar{p}p \rightarrow \pi^-\pi^+$ likewise finds an f_2 resonance at 1996 MeV. We have tried an alternative fit using instead $f_2(1920)$ observed by both GAMS [21] and VES [22] collaborations. The $2^{++} \rightarrow a_2\pi$ partial wave can be reproduced equally well with this assignment, but the $2^{++} \rightarrow f_2\eta$ partial wave is seriously underfitted by a factor 3 at 2050 MeV, ruling out a fit by $f_2(1920)$ only.

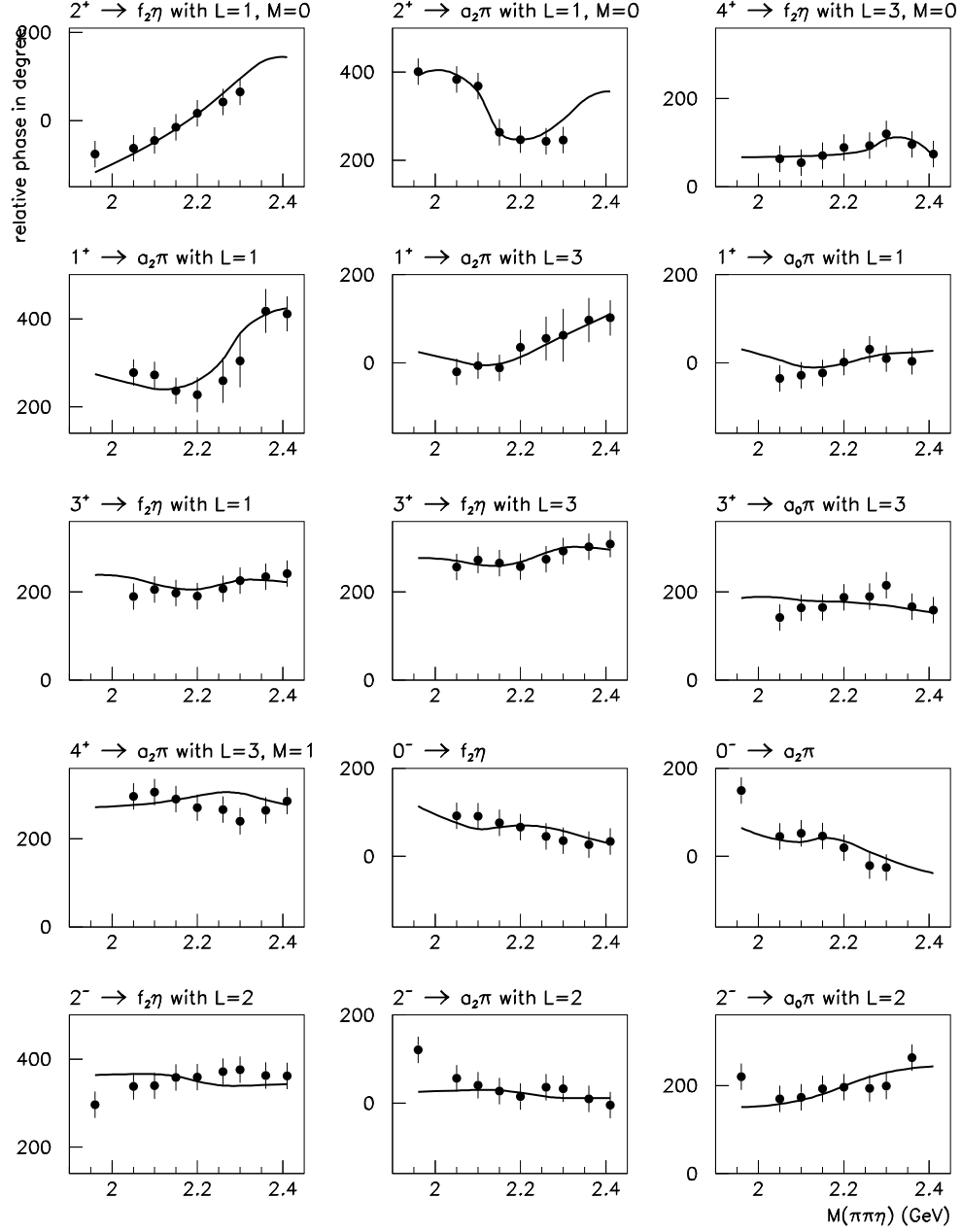


Figure 13: Relative phases (data points with error bars) obtained from the partial wave analysis and used for the fit (curves) to get Argand plots together with masses and widths of the resonances. The phases for 2^+ and 4^+ with $M=0$ are relative to $4^+ \rightarrow a_2\pi$ with $L=3$ and $M=0$; the phases for 1^+ , 3^+ and 4^+ with $M=1$ are relative to $4^+ \rightarrow f_2\eta$ with $L=3$ and $M=1$; the phases for 0^- and 2^- are relative to $2^- \rightarrow f_2\eta$ with $L=0$.

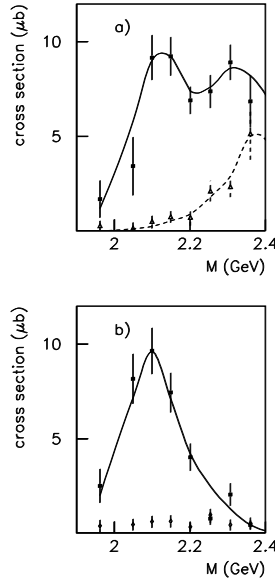


Figure 14: Contributions to (a) $f_2(1270)\eta$, (b) $a_2(1320)\pi$ from 3F_4 (black squares) and 3H_4 (open triangles).

The proximity of this resonance to $f_4(2050)$ suggests that it may be identified as the $\bar{q}q$ 3F_2 state expected near this mass. Because 2^+ amplitudes with $M = 1$ are negligible, 3P_2 and 3F_2 amplitudes have the same s -dependence; 3F_2 is the larger by a factor 1.44. This strong coupling of $f_2(2030)$ to $\bar{p}p$ 3F_2 also suggests identification with $\bar{q}q$ 3F_2 : high L in $\bar{q}q$ is likely to be associated with high L in decay channels, because of the peaking of wave functions at large r .

At higher masses, a fit with a single resonance, shown by the dashed curve in Fig. 16, is much poorer than with two separate resonances. The peak at 2240 MeV in $f_2(1270)\eta$ has a mass compatible with $\xi(2230)$ observed in J/Ψ radiative decays [23], but has a larger width of about 170 MeV. This resonance may be interpreted as the $n = 4$ $\bar{q}q$ 3P_2 state, in the sequence $f_2(1270)$, $f_2(1565)$, $f_2(1920)$, $f_2(2240)$. The $f_2(2370)$ finds a natural explanation as $n = 2$ $\bar{q}q$ 3F_2 , i.e. the radial excitation of $f_2(2020)$. Its strong $L = 3$ decay supports this interpretation. In present data, both $f_2(2240)$ and $f_2(2370)$ appear in both 3P_2 and 3F_2 , suggesting mixing between these states.

The two peaks around 2020 MeV and 2370 MeV have masses and widths compatible with $f_2(2010)$ and $f_2(2340)$ listed by the PDG [4]. However, those observations were in the $\phi\phi$ channel and could be different resonances, e.g. $\bar{s}s$. We also remark that the peak in the $\phi\phi$ data of Etkin et al. [24] actually appears at ~ 2150 MeV. It is the rapid opening of the $\phi\phi$ phase space which leads to a pole at much lower mass, 2020 MeV, in the K-matrix fit to their data.

4.4 $J^P = 1^+$

For $J^{PC} = 1^{++} \rightarrow a_2(1320)\pi$ and $a_0(980)\pi$, there is a peak at the lowest masses. This suggests a resonance close to or below the $\bar{p}p$ threshold. However, as discussed below, the phase variation of the 1^+ amplitude provides evidence for a resonance around 2340 MeV. The phase variation shown in Fig. 15 obviously requires resonant activity in the mass range 2000–2400 MeV.

4.5 $J^P = 2^-$

Partial waves with quantum numbers 2^{-+} and 0^{-+} correspond to $\bar{p}p$ singlet states, and therefore there is no interference with even parity (triplet) partial waves. For 2^{-+} there is a strong peak in $f_2(1270)\eta$ at ~ 2050 MeV and a smaller peak in $a_2(1320)\pi$ at similar mass. There is evidence for a further peak at ~ 2300 MeV. The

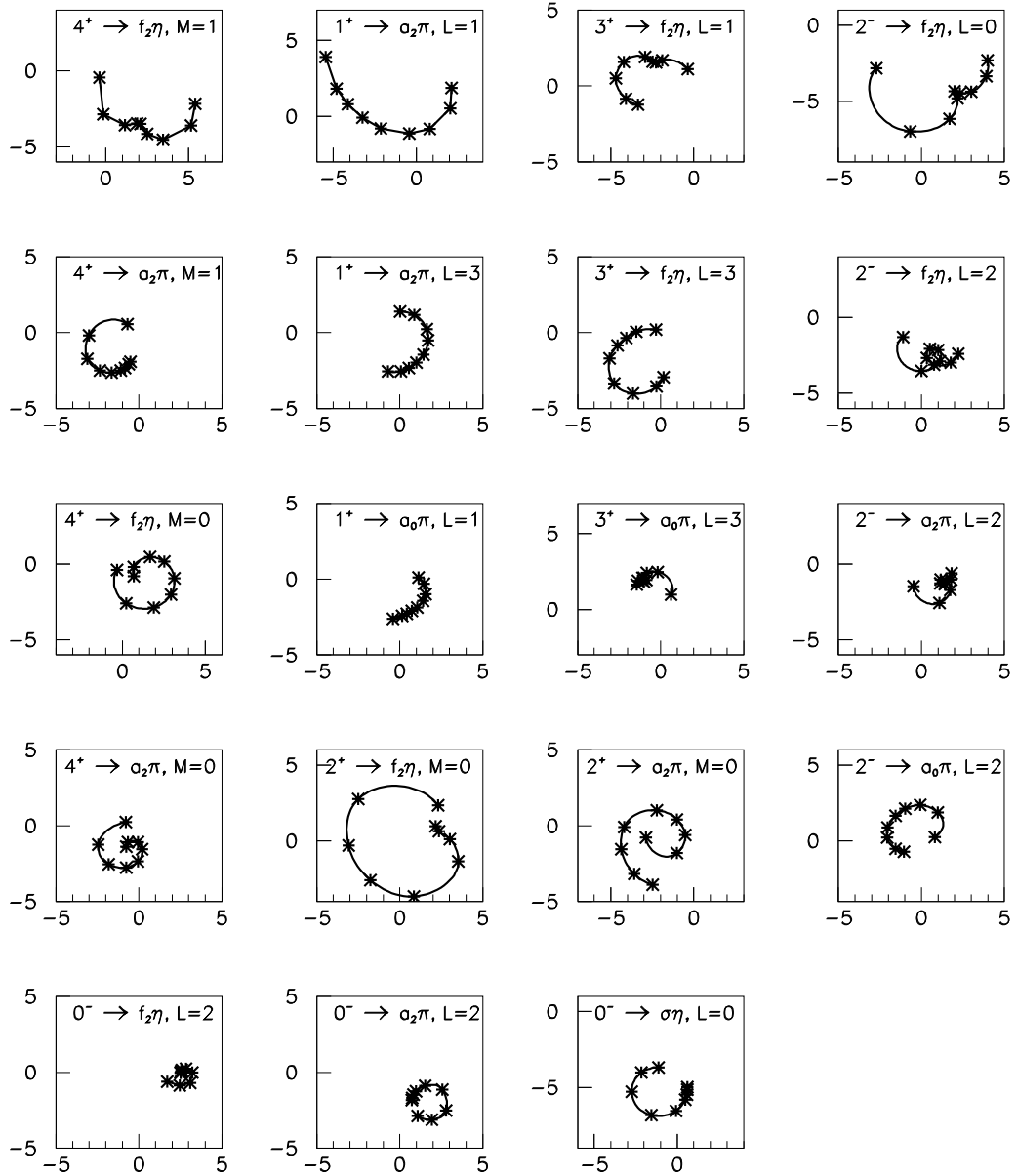


Figure 15: Argand plots corresponding to curves in Figs.11 and 13.

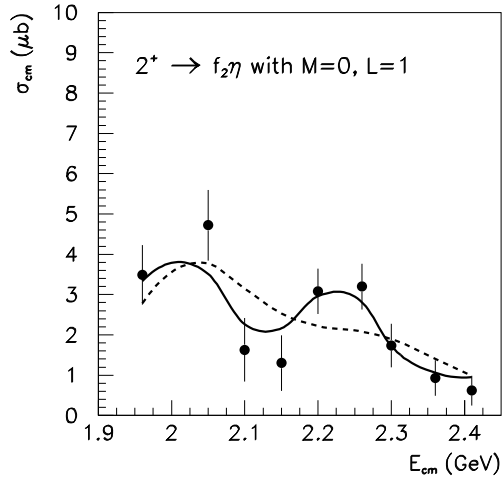


Figure 16: Fits with $f_2(2240)$ (full curve) and without (dashed).

lower peak is well fitted by a resonance with $M = 2040 \pm 40$ MeV. The almost 360° phase advance observed on the Argand diagram points strongly towards the presence of two resonances, the second at 2300 ± 40 MeV. The PDG does not list any $I = 0$ $J^{PC} = 2^{-+}$ resonance in this mass range. A possible $I = 1$ partner is listed in the form of $\pi_2(2100)$.

4.6 $J^P = 0^-$

For 0^{-+} , there is a broad, slowly varying intensity with evidence for a strong peak superimposed at $M \sim 2140$ MeV. The slowly varying component may correspond to the broad 0^{-+} object used in describing J/Ψ radiative decays to $\rho\rho$, $\omega\omega$, $K^*\bar{K}^*$, $\phi\phi$ and $\eta\pi\pi$ [25]. The peak at 2140 MeV may correspond to a narrow resonance. However, it is observed in the $\eta\sigma$ channel, which contributes across the entire Dalitz plot. This contribution might absorb weak components not presently fitted to the data, for example due to $a_0(1450)$, $a_2(1660)$, $\hat{\rho}(1405)$ or further resonances in the production process around 2 GeV. In view of this possibility, the interpretation in terms of a resonance is ambiguous. Unfortunately, the relative phase with respect to 2^- is not well determined, so the phase variation cannot be used for independent evidence of resonant activity.

5 Final fit to the partial waves

To get more precise values for masses and widths for resonances, we use interfering sums of the Breit-Wigner amplitudes to fit the partial wave cross sections in Fig.11 and the relative phases of the partial waves in Fig.13 simultaneously. The fit is shown in Figs. 11-13 as full curves.

Besides the obvious resonances mentioned in the previous section, we need another 1^{++} resonance at about 2340 MeV with width ~ 340 MeV. Without it, we cannot describe the relative phase between 1^{++} and 4^{++} partial waves; also we would need the lower 1^{++} resonance to be very narrow (< 50 MeV) in order to explain the sharply decreasing 1^{++} partial wave cross section. In our present fit with two 1^{++} resonances, the $f_1(2340)$ amplitude interferes destructively with the tail of the lower 1^{++} resonance and causes the sharply decreasing cross section with a broad dip around 2340 MeV. The phase motion caused by this $f_1(2340)$ can be seen clearly in the Argand plots for 1^{++} partial waves of Fig.15.

In Table 2, the branching ratios are calculated at the resonance masses and are corrected for their unseen decay modes, except for $a_0(980)$ where $\Gamma_{a_0\pi} = \Gamma_{a_0\pi \rightarrow \eta\pi\pi}$.

For an ordinary $q\bar{q}$ state, the relative ratio $f_2\eta/a_2\pi$ is expected to be smaller than 0.64. This allows for the 36% component of $\bar{s}s$ in the η . The centrifugal barrier and phase space will further suppress $f_2\eta$. Most of the branching ratios in Table 2 are in qualitative agreement with what is expected for $\bar{q}q$ states. However, the $f_2(2230)$ has an anomalously strong branching ratio to $f_2(1270)\eta$ compared with $a_2(1320)\pi$.

For the well-established $f_4(2050)$, only 44% of its branching ratios are listed in the Particle Data Tables [4], in which $\pi\pi$ has a branching ratio of $(17 \pm 1.5)\%$. In a very recent analysis [26] of $\bar{p}p \rightarrow \pi\pi$, the ratio $\frac{\Gamma_{\bar{p}p}\Gamma_{\pi\pi}}{\Gamma_{tot}}$ was reported to be $(2.2 \sim 2.4) \times 10^{-3}$. Using this information, we can get the branching ratios of $f_4(2050)$ to $\bar{p}p$, $a_2\pi$ and $f_2\eta$ to be $(1.4 \pm 0.1)\%$, $(30 \pm 5)\%$ and $(3.9 \pm 1.0)\%$, respectively.

5.1 Comments on the resonance spectrum

The $f_4(2044)$, $f_3(2000)$, $f_2(2020)$ and $\eta_2(2040)$ cluster closely into a tower of resonances, as anticipated in the Veneziano model. Likewise the $f_4(2320)$, $f_3(2280)$, $f_2(2370)$, $f_1(2340)$ and $\eta_2(2300)$ show indications of clustering into a tower at the higher masses.

The $f_2(1920)$ originally discovered by both GAMS and VES has recently been confirmed in further VES data with increased statistics, decaying to $\omega\omega$ [20]. There is also a strong $f_2(1270)\eta$ signal in VES $\eta\pi^+\pi^-$ data. Together with the $f_2(2020)$ we observe here, $f_2(2240)$ and $f_2(2370)$, this tentatively completes the identification of the $\bar{q}q$ $I = 0$ 3P_2 and 3F_2 states expected in this mass range.

We conclude with some speculative suggestions of a scheme which concerns mixing of $\bar{q}q$ states with the 2^+ glueball expected in this mass range. In our data on $\bar{p}p \rightarrow \eta\eta\pi^0$ [2], there is evidence for a further broad $f_2(1980)$ decaying to $\eta\eta$, with mass $M = 1980 \pm 50$ MeV, $\Gamma = 500 \pm 100$ MeV. Its effects are seen clearly down to masses of ~ 1550 MeV. There is also evidence for a broad 2^+ resonance in 4π final states in central production [27]. Such a broad state was predicted by Bugg and Zou [25]. It may be interpreted as a mixed state formed from the 2^+ glueball, expected at $\sim 2 - 2.2$ GeV, and nearby $\bar{q}q$ states. Anisovich et al. [28] have argued that this mixing will lead to a broad state, accumulating the widths of nearby $\bar{q}q$ states and making them narrower. The $f_2(1920)$ and $f_2(2240)$ are indeed somewhat narrower this is usual for resonances in this mass range. Mixing with a glueball provides a natural explanation of the anomalous decays of $f_2(2020)$ and $f_2(2340)$ to $\phi\phi$, observed by Etkin et al. [24].

The glueball may be small, with radius ~ 0.3 fm; there are indications for this small radius in QCD Lattice calculations [29]. The small radius allows much of the glueball mass to be attributed to zero-point energy. Such a small object will mix preferentially with $\bar{q}q$ 3P_2 states rather than $\bar{q}q$ 3F_2 , whose wave functions are strongly localised at large r . The preferential decays of $f_2(1920)$ and $f_2(2240)$ to $f_2(1270)\eta$, despite its smaller phase space than $a_2(1320)\pi$, may be a further indication of mixing with the 2^+ glueball.

6 Summary

In summary, we have observed a new decay mode $\eta\pi\pi$ for $f_4(2050)$. In addition, we have evidence for 7 new or poorly established resonances in the energy range from 1.96 to 2.41 GeV, i.e., $f_4(2320)$, $f_3(2000)$, $f_3(2280)$, $f_2(2240)$, $f_1(2340)$, $\eta_2(2040)$ and $\eta_2(2300)$. They appear to cluster into two towers of resonances around 2000–2050 MeV and 2300 MeV. Results are broadly consistent with earlier evidence for $f_4(2300)$, $f_2(2020)$ and $f_2(2340)$.

7 Acknowledgement

We thank the Crystal Barrel Collaboration for allowing use of the data. We also thank the technical staff of the LEAR machine group and of all the participating institutions for their invaluable contributions to the success of the experiment. We acknowledge financial support from the the British Particle Physics and Astronomy Research Council (PPARC). The St.Petersburg group thanks INTAS for financial support, contract RFBR 95-0267, and also PPARC for financial assistance for collaborative work.

References

- [1] A. Anisovich et al., *Study of $\bar{p}p \rightarrow \pi^0\pi^0\eta$ from 600 to 1940 MeV/c*.

- [2] A. Anisovich et al., *Study of the process $\bar{p}p \rightarrow \eta\eta\pi^0$ from 1350 to 1940 MeV/c*, Phys. Lett. B449 (1999) 145.
- [3] A. Anisovich et al., *Observation of $f_0(1770) \rightarrow \eta\eta$ in $\bar{p}p \rightarrow \eta\eta\pi^0$ reactions from 600 to 1940 MeV/c*, Phys. Lett. B 449 (1999) 154.
- [4] Particle Data Group, C. Caso et al., Euro. Phys. J. C3 (1998) 1.
- [5] A.Hasan et al., Nucl. Phys. B378 (1992) 3.
- [6] A.Hasan and D.V.Bugg, Phys. Lett. B334 (1994) 215.
- [7] G. Veneziano, Nu. Cim. 57A (1968) 190.
- [8] G.Bali et al. (UKQCD), Phys. Lett. **B307** (1993) 378; H.Chen, J.Sexton, A.Vaccarino and D.Weingarten, Nucl. Phys. B (Proc. Suppl.) 34 (1994) 357.
- [9] V.A.Novikov, M.A.Shifman, A.I.Vainshtein and V.I.Zakhnov, Nucl. Phys. B 191 (1981) 301.
- [10] J.Y.Cui, J.M.Wu and H.Y.Jin, Phys. Lett. B424 (1998) 381.
- [11] V.V. Anisovich et al., Phys. Lett. B323 (1994) 233; C. Amlser et al., Phys. Lett. B355 (1995) 425.
- [12] D.V.Bugg et al., Phys. Lett. **B353** (1995) 378.
- [13] E. Aker et al., Nucl. Instr. A321 (1992) 69.
- [14] C.A. Baker, N.P Hesse, C.N. Pinder and C.J. Batty, Nucl. Instr. and Methods in Phys. Res. A394 (1997) 180.
- [15] A. Anisovich et al., *$\bar{p}p \rightarrow \pi^0\pi^0$ from 600 to 1940 MeV/c*, submitted to Phys. Lett. B.
- [16] A.Bertin et al., Phys. Rev. D57 (1998) 55.
- [17] S.U.Chung, Phys. Rev. D48 (1993) 1225; D57 (1998) 431.
- [18] D.V.Bugg, A.V.Sarantsev and B.S.Zou, Nucl. Phys. B471 (1996) 59.
- [19] D. Ryabchikov, AIP Conf. Proc. 432, eds. S.-U. Chung and H.J. Willutzki, (Amer. Inst. of Phys. New York, 1998), p603.
- [20] D. Ryabchikov, private communication.
- [21] D. Alde et al., Phys. Lett. B276 (1992) 375.
- [22] S.I.Beladidze et al., Z.Phys. C54 (1992) 367.
- [23] BES collaboration, J.Z.Bai et al., Phys. Rev. Lett. 76 (1996) 3502.
- [24] A. Etkin et al., Phys. Lett. B201(1988) 568.
- [25] D.V.Bugg and B.S.Zou, Phys. Lett. B396 (1997) 295.
- [26] B.R.Martin and G.C.Oades, Preprint IFA-SP-98-1, HEPPH-9802261.
- [27] D. Barberis et al., Phys. Lett. B413 (1997) 217.
- [28] V.V. Anisovich, D.V. Bugg and A.V. Sarantsev, hep-ph/9711478 (1997) and Phys. Lett B (to be published).
- [29] D. Weingarten, private communication.